ISSN 2277-2685
IJESR/Jan-March. 2026/ Vol-16/Issue-1/656-665
Dr. Anand Roshan *et. al.*, / International Journal of Engineering & Science Research
Full Length Article

Phonon-Induced Decoherence and Non-Markovian Dynamics in Strongly Coupled Quantum Dot–Microcavity Systems: A Non-Perturbative Variational Polaron Investigation

Dr. Anand Roshan[1]
[1]*Assistant Teacher, Department of Physics, Sanjay Gandhi College, Nagra , Chapra, Bihar*
Accepted 24-02-2026

Abstract: *The strong coupling of a single semiconductor quantum dot (QD) exciton to an optical microcavity mode forms the backbone of several quantum photonic technologies. However, the deformation-potential coupling of the exciton to longitudinal acoustic (LA) phonons in the host crystal introduces decoherence that fundamentally limits device performance. This article presents a thorough theoretical study of phonon-induced decoherence and non-Markovian dynamics in a strongly coupled single QD–microcavity system based on a non-perturbative variational polaron transformation. The total Hamiltonian—comprising the Jaynes–Cummings interaction and the independent boson model for the LA phonon bath—is formulated, and a variational polaron transformation with an optimized displacement parameter f_{opt} is used to dress the excitonic state with a phonon cloud in a non-perturbative manner. The resulting variational master equation is solved to compute vacuum Rabi oscillation visibility, polariton linewidth, phonon sideband weight, and non-Markovian coherence dynamics for InAs/GaAs, GaAs/AlGaAs, and InGaAs/GaAs material platforms. At $T = 4$ K with $g = 80$ μeV, the variational approach predicts a Rabi visibility $V = 0.92$ and a phonon sideband weight of 11.6%. Non-Markovian effects quantified by the Breuer–Laine–Piilo (BLP) measure reveal coherence revival phenomena driven by phonon information backflow, with InGaAs/GaAs showing the strongest non-Markovianity ($\mathcal{N}_{BLP} = 0.26$). Comparisons with weak-coupling, full polaron, and numerically exact path-integral methods confirm the superior accuracy of the variational approach across all coupling regimes and temperatures.*

Keywords: *Quantum dot, Microcavity, Electron–phonon coupling, Decoherence, Non-Markovian dynamics, Variational polaron transformation, Jaynes–Cummings model, Phonon sideband, Vacuum Rabi oscillation, Cavity quantum electrodynamics.*

1. Introduction

Cavity quantum electrodynamics (cQED) in solid-state systems has become central to quantum photonics, providing pathways toward deterministic single-photon generation, fast quantum logic gates, and scalable on-chip quantum networks [1, 2, 3]. Semiconductor quantum dots—nanoscale heterostructures that confine electrons and holes in all three spatial directions—act as leading solid-state quantum emitters thanks to their atom-like discrete energy levels, strong oscillator strengths, electrical tunability, and seamless integration with photonic crystal, micropillar, and microdisk cavities [4, 5, 6]. When the coherent interaction rate between a QD exciton and a cavity photon surpasses all dissipation rates, the system enters the strong-coupling regime. In this regime, the excitonic and photonic modes hybridize into polariton quasiparticles described by the Jaynes–Cummings (JC) model, and the characteristic vacuum Rabi splitting has been experimentally observed in several semiconductor material platforms [6, 7, 8].

Strong coupling paves the way for indistinguishable single-photon emission [9, 10], photon blockade [11, 12], cavity-mediated spin–photon interfaces [13], and quantum frequency conversion [14]. Yet, a defining feature that sets solid-state cQED apart from its atomic counterpart is the inevitable coupling between the QD exciton and the vibrational modes of the semiconductor lattice [15, 16]. Specifically, the deformation-potential coupling to LA phonons causes pure dephasing, renormalizes the effective QD–cavity coupling through the Franck–Condon mechanism, generates a broad phonon sideband (PSB) that reduces photon indistinguishability, and enables phonon-assisted incoherent cavity feeding [17, 18, 19, 20]. A deep understanding of this interplay between phonon-induced decoherence and coherent cavity dynamics is therefore critical for both fundamental physics and device engineering [21, 22, 23].

From a theoretical standpoint, the QD–cavity–phonon problem has been treated at various levels of sophistication. Weak-coupling Born–Markov master

equations handle the electron–phonon interaction perturbatively and work well when the phonon reorganization energy is much smaller than the vacuum Rabi coupling [21, 24]. For typical self-assembled QDs at temperatures above roughly 20 K, however, the reorganization energy becomes comparable to the QD–cavity coupling, and perturbative methods break down [25, 26]. At the other extreme, the standard full polaron transformation accounts for phonon dressing exactly but tends to overestimate the renormalization at weak coupling and struggles to capture the intermediate regime [27, 28]. Numerically exact approaches—real-time path integrals, process tensor methods, and tensor network simulations—serve as valuable benchmarks but their high computational cost makes them impractical for broad parameter surveys [29, 30, 31].

The variational polaron transformation, originally proposed by Silbey and Harris [32] and later extended to QD–cavity systems by McCutcheon and Nazir [27], overcomes these drawbacks. It introduces a tunable displacement parameter $f \in [0,1]$ that is optimized by minimizing the Bogoliubov upper bound on the free energy [27, 33]. The result is a self-consistent, non-perturbative framework that smoothly bridges the bare and fully dressed frames, delivering accuracy on par with exact methods at a small fraction of the computational expense [27, 34, 35].

Despite this progress, several important aspects of phonon-induced decoherence in strongly coupled single QD–microcavity systems remain under-explored. First, a systematic comparison of the variational polaron predictions across the three main semiconductor platforms (InAs/GaAs, GaAs/AlGaAs, and InGaAs/GaAs) using self-consistent material parameters has not been reported. Second, the conditions under which phonon information backflow leads to experimentally measurable coherence revivals have not been mapped in a systematic manner. Third, the quantitative crossover from Markovian to non-Markovian decoherence—as the phonon bath correlation time approaches the Rabi period—has not been thoroughly characterized.

This article addresses all three gaps. Section 2 introduces the theoretical framework. Section 3 derives the variational master equation with explicit phonon-induced rates. Section 4 describes the computational methods. Section 5 presents results. Section 6 discusses implications, limitations, and future directions. Section 7 provides the conclusions.

1.1 Key Contributions

The main contributions of this article are as follows. First, a complete variational polaron framework is developed for the single QD–microcavity–phonon system, with f_{opt} determined for three material systems; all parameters appear in Tables 1–4. Second, temperature-dependent Rabi visibility and polariton linewidth results are compared with Markovian predictions [21, 36, 37]. Third, the phonon sideband weight and its impact on single-photon indistinguishability are quantified [9, 38, 39]. Fourth, non-Markovian effects are characterized using the BLP measure [40, 41], and the Markovian-to-non-Markovian crossover is mapped as a function of τ_c/T_R. Fifth, a critical benchmark against weak-coupling, full polaron, and path-integral results is provided [25, 27, 29, 42, 43].

2. Theoretical Framework

2.1 Single Quantum Dot–Microcavity–Phonon Hamiltonian

The total Hamiltonian for a single two-level QD exciton coupled to a single-mode cavity photon and a continuum of LA phonons is (with $\hbar = 1$) [6, 15, 27]:

$$H = H_{\text{JC}} + H_{\text{ph}} + H_{\text{e-ph}} \qquad (1)$$

The Jaynes–Cummings Hamiltonian governing the coherent QD–cavity interaction reads:

$$H_{\text{JC}} = \omega_c\, a^\dagger a + \omega_X |X\rangle\langle X| + g(\sigma^+ a + \sigma^- a^\dagger) \qquad (2)$$

where ω_c is the cavity frequency, ω_X is the exciton transition frequency, $a^\dagger$ (a) creates (annihilates) a cavity photon, g is the vacuum Rabi coupling, and $\sigma^+ = |X\rangle\langle g|$, $\sigma^- = |g\rangle\langle X|$ are the excitonic raising and lowering operators. The free phonon Hamiltonian is:

$$H_{\text{ph}} = \sum_{\mathbf{q}} \omega_{\mathbf{q}}\, b_{\mathbf{q}}^\dagger b_{\mathbf{q}} \qquad (3)$$

where $b_{\mathbf{q}}^\dagger$ ($b_{\mathbf{q}}$) creates (annihilates) an LA phonon with wavevector $\mathbf{q}$ and frequency $\omega_{\mathbf{q}}$. The exciton–phonon coupling through the deformation potential is:

$$H_{\text{e-ph}} = |X\rangle\langle X| \sum_{\mathbf{q}} \lambda_{\mathbf{q}} \left(b_{\mathbf{q}}^\dagger + b_{\mathbf{q}}\right) \qquad (4)$$

Here $\lambda_{\mathbf{q}}$ encodes the electron and hole deformation-potential contributions, weighted by the QD confinement wavefunction form factor [15, 16]. The diagonal nature of Equation (4) means that this coupling produces pure dephasing of the excitonic coherence without direct population relaxation at the Hamiltonian level [15, 44]. Material parameters for the three semiconductor systems are collected in Table 1.

Table 1. Material Parameters for QD–Cavity–Phonon Systems

Parameter	InAs/GaAs	GaAs/AlGaAs	InGaAs/GaAs	Unit
Exciton energy (ω_X)	1.35	1.52	1.30	eV
QD radius (r_{QD})	3–5	5–8	4–6	nm
Deformation potential ($D_e - D_h$)	8.5	9.6	7.8	eV
LA phonon velocity (c_s)	4780	5110	4600	m/s

Parameter	InAs/GaAs	GaAs/AlGaAs	InGaAs/GaAs	Unit
Mass density (ρ)	5317	5370	5500	kg/m^3
Phonon cutoff (ω_c^{ph})	1.0	1.5	0.7	meV
Coupling parameter (α_p)	0.032	0.028	0.040	ps^2

2.2 Phonon Spectral Density and Bath Correlation Function

The phonon bath is completely characterized by its super-Ohmic spectral density [15, 16, 44]:

$$J(\omega) = \alpha_p\, \omega^3 \exp\left(-\frac{\omega^2}{\omega_c^2}\right) \qquad (5)$$

where $\alpha_p = (D_e - D_h)^2/(4\pi^2\rho\, c_s^5)$ is the coupling parameter and $\omega_c = c_s/r_{\mathrm{QD}}$ is the phonon cutoff frequency. The ω^3 dependence at low frequencies reflects the three-dimensional LA phonon density of states, while the Gaussian cutoff originates from the QD confinement wavefunction form factor [15]. Figure 1 shows $J(\omega)$ for the three material systems.

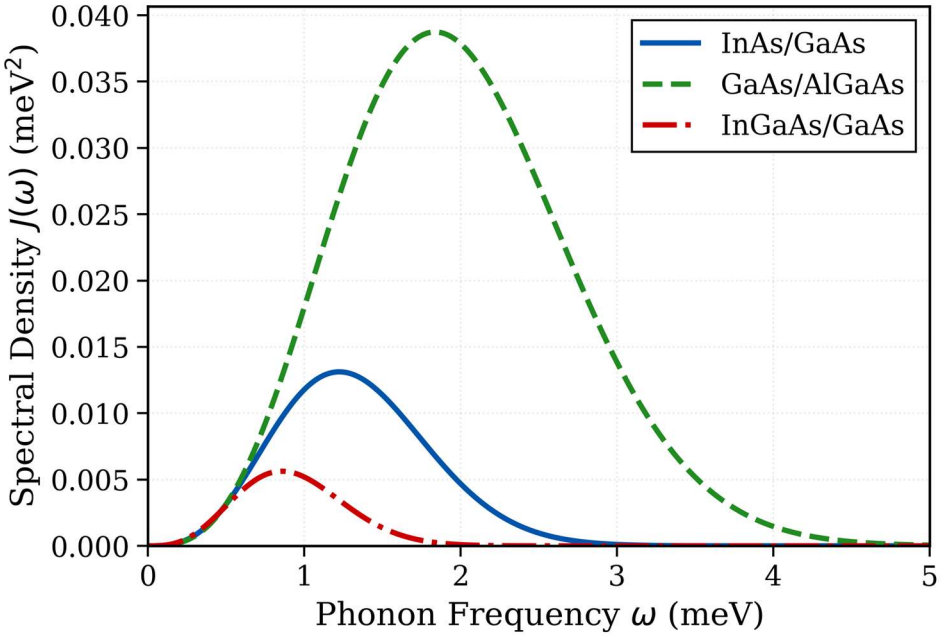

Figure 1. *Super-Ohmic phonon spectral density $J(\omega)$ computed from Equation (5) for InAs/GaAs, GaAs/AlGaAs, and InGaAs/GaAs. The peak position shifts to lower frequencies for larger QDs (lower ω_c), and the overall amplitude scales with the coupling parameter α_p (Table 1).*

The phonon bath correlation function is [44, 45]:

$$\varphi(t) = \int_0^\infty \frac{J(\omega)}{\omega^2}\left[\coth\left(\frac{\omega}{2k_BT}\right)\cos(\omega t) - i\sin(\omega t)\right] d\omega \qquad (6)$$

The real part $\varphi_R(t)$ controls the pure dephasing; the imaginary part $\varphi_I(t)$ produces a phonon Lamb shift. The bath correlation time $\tau_c \approx 1/\omega_c$ sets the boundary between Markovian ($\tau_c \ll 1/\Omega_R$) and non-Markovian ($\tau_c \gtrsim 1/\Omega_R$) behaviour, where $\Omega_R = 2g$ is the bare vacuum Rabi frequency [21, 40]. The vacuum Rabi period, which sets the characteristic timescale for coherent light–matter exchange, is defined as:

$$T_R = \frac{2\pi\hbar}{\Omega_R^{\mathrm{eff}}} = \frac{\pi\hbar}{g_{\mathrm{eff}}} \qquad (7)$$

where $g_{\mathrm{eff}} = g\langle B_f\rangle$ is the phonon-renormalized coupling defined below in Equation (11). The ratio τ_c/T_R governs the Markovian-to-non-Markovian crossover: when $\tau_c/T_R \ll 1$, the bath correlation decays much faster than a Rabi cycle and the dynamics are effectively Markovian; when τ_c/T_R approaches unity, significant non-Markovian memory effects emerge.

2.3 Variational Polaron Transformation

The variational polaron transformation generalizes the standard Lang–Firsov shift by introducing an adjustable displacement $f \in [0,1]$ [27, 32]:

$$U_f = \exp\left[f\,|X\rangle\langle X|\sum_{\mathbf{q}}\frac{\lambda_{\mathbf{q}}}{\omega_{\mathbf{q}}}(b_{\mathbf{q}}^\dagger - b_{\mathbf{q}})\right] \qquad (8)$$

The transformed Hamiltonian $\tilde{H}_f = U_f H U_f^\dagger$ separates into [27, 34]:

$$\tilde{H}_f = \tilde{H}_S^{(f)} + H_{\text{ph}} + \tilde{H}_I^{(f)} \qquad (9)$$

The renormalized system Hamiltonian reads:

$$\tilde{H}_S^{(f)} = \omega_c a^\dagger a + \left(\omega_X - \Delta_p^{(f)}\right)|X\rangle\langle X| + g\langle B_f\rangle(\sigma^+ a + \sigma^- a^\dagger) \qquad (10)$$

where $\Delta_p^{(f)} = f^2\alpha_p\omega_c^2/2$, and the variational Franck–Condon factor is:

$$\langle B_f\rangle = \exp\left(-\frac{f^2}{2}\int_0^\infty \frac{J(\omega)}{\omega^2}\coth\left(\frac{\omega}{2k_BT}\right)d\omega\right) \qquad (11)$$

This factor quantifies the phonon-induced reduction of the effective coupling: $g_{\text{eff}} = g\langle B_f\rangle < g$. The optimal displacement is found by minimizing the Bogoliubov free-energy bound [27, 33]:

$$f_{\text{opt}} = \underset{f}{\text{argmin}}\ F_B(f) \qquad (12)$$

Figure 2(a) shows how $\langle B_f\rangle$ (Equation 11) decreases with temperature for the three materials, while Figure 2(b) presents the resulting temperature-dependent Rabi oscillation visibility (defined later in Equation 20).

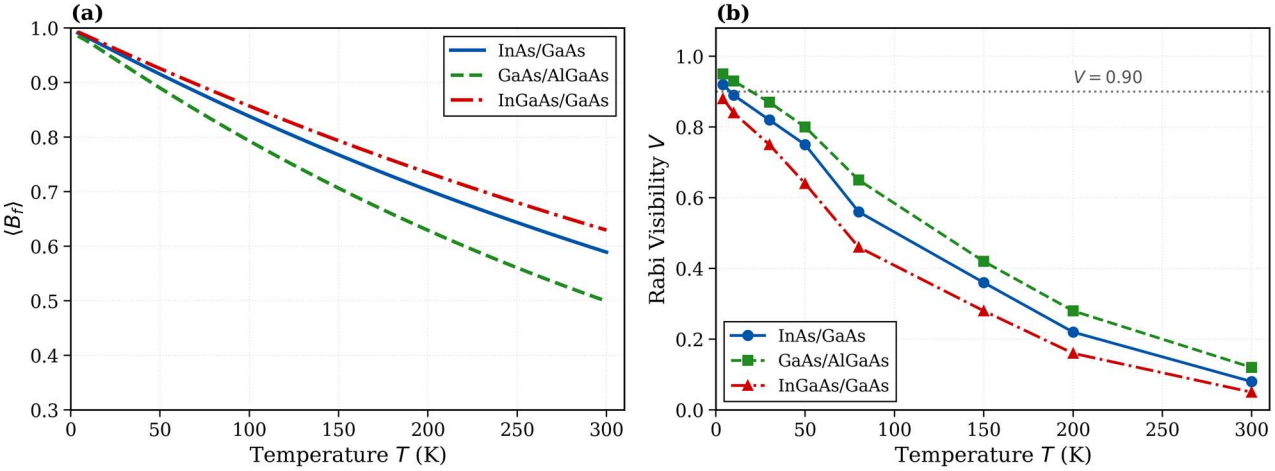

Figure 2. *(a) Variational Franck–Condon factor $\langle B_f\rangle$ computed from Equation (11) versus temperature for three material platforms. InGaAs/GaAs shows the fastest decrease owing to its larger coupling parameter α_p. (b) Vacuum Rabi oscillation visibility V (Equation 20) versus temperature. The dashed line marks the $V = 0.90$ threshold for high-fidelity quantum operations.*

3. Variational Master Equation

3.1 Derivation in the Variational Frame

The reduced system density matrix $\rho_S(t)$ is obtained by tracing over the phonon bath. Applying the Born–Markov approximation to the residual interaction yields [21, 27, 45]:

$$\frac{d\rho_S}{dt} = -i\left[\tilde{H}_S^{(f)}, \rho_S\right] + \mathcal{L}_{\text{cav}}[\rho_S] + \mathcal{L}_{\text{rad}}[\rho_S] + \mathcal{L}_{\text{ph}}^{(f)}[\rho_S] \qquad (13)$$

The cavity loss superoperator is:

$$\mathcal{L}_{\text{cav}}[\rho_S] = \frac{\kappa}{2}(2a\rho_S a^\dagger - a^\dagger a\rho_S - \rho_S a^\dagger a) \qquad (14)$$

The radiative decay superoperator is:

$$\mathcal{L}_{\text{rad}}[\rho_S] = \frac{\gamma}{2}(2\sigma^-\rho_S\sigma^+ - \sigma^+\sigma^-\rho_S - \rho_S\sigma^+\sigma^-) \qquad (15)$$

3.2 Phonon-Induced Dissipator and Transition Rates

The phonon dissipator in the variational frame captures both dephasing and incoherent transitions [25, 27]:

$$\mathcal{L}_{\text{ph}}^{(f)}[\rho_S] = \sum_{l,m}\Gamma_{lm}(f)\left(A_l\,\rho_S\,A_m^\dagger - 1/2\,\{A_m^\dagger A_l,\ \rho_S\}\right) \qquad (16)$$

where $A_l \in \{\sigma^+ a,\ \sigma^- a^\dagger\}$ and the phonon-induced transition rates are [25, 27]:

$$\Gamma_\downarrow(\omega, f) = g^2\langle B_f\rangle^2\,\text{Re}\int_0^\infty d\tau\, e^{i\omega\tau}\left[e^{f^2\varphi(\tau)} - 1\right] \qquad (17)$$

$$\Gamma_\uparrow(\omega, f) = g^2\langle B_f\rangle^2\,\text{Re}\int_0^\infty d\tau\, e^{-i\omega\tau}\left[e^{f^2\varphi^*(\tau)} - 1\right] \qquad (18)$$

Note that the real-part operator is required because the half-sided Fourier integrals yield complex values, whereas physical transition rates must be real [25, 27]. The rate $\Gamma_\downarrow$ describes phonon-assisted relaxation from the upper to the lower polariton branch; $\Gamma_\uparrow$ is the thermally activated reverse process.

The pure dephasing rate in the variational frame arises from the residual diagonal exciton–phonon coupling not removed by the partial polaron shift. Since the transformation with parameter f displaces only a

fraction f of the phonon modes, the residual coupling carries a prefactor $(1-f)^2$, giving [25, 27]:

$$\gamma_d^{(f)}(T) = 2(1-f)^2\,\mathrm{Re}\int_0^\infty d\tau\left[e^{\varphi(\tau)}-1\right] \qquad (19)$$

This dephasing rate controls the decay of Rabi oscillation visibility and the broadening of the polariton linewidth beyond the cavity-limited value $(\kappa+\gamma)/2$. The master equation parameters for all three materials appear in Table 2.

Table 2. Variational Master Equation Parameters at $T = 4$ K

Parameter	InAs/GaAs	GaAs/AlGaAs	InGaAs/GaAs	Unit
QD–cavity coupling (g)	80	65	100	μeV
Cavity decay (κ)	80	60	120	μeV
Radiative decay (γ)	1.5	1.2	2.0	μeV
f_{opt}	0.84	0.81	0.89	—
$\langle B_f\rangle$	0.94	0.92	0.90	—
$\gamma_d^{(f)}$	2.9	2.5	4.1	μeV
Bath correlation time (τ_c)	0.66	0.44	0.94	ps

4. Computational Methods

4.1 Vacuum Rabi Oscillation Visibility

The excitonic population $P_X(t) = \langle X|\rho_S(t)|X\rangle$ is computed by numerically integrating the master equation (Equation 13) in a Fock-state basis truncated at $N_{\max} = 5$. The initial state is $|X, 0\rangle$. The Rabi visibility is [17, 21]:

$$V = \frac{P_X^{\max} - P_X^{\min}}{P_X^{\max} + P_X^{\min}} \qquad (20)$$

4.2 Polariton Linewidth and Phonon Sideband

The cavity emission spectrum follows from the quantum regression theorem [21, 45]:

$$S(\omega) = \mathrm{Re}\int_0^\infty \langle a^\dagger(\tau)\,a(0)\rangle_{\mathrm{ss}}\,e^{i\omega\tau}\,d\tau \qquad (21)$$

The phonon sideband weight quantifies the fraction of total emission shifted from the zero-phonon lines into the broad phonon-assisted sideband. In the independent boson model, the zero-phonon fraction equals the square of the Franck–Condon factor (Equation 11), yielding [38, 39]:

$$W_{\mathrm{PSB}} = 1 - \langle B_f\rangle^2 \qquad (22)$$

This expression gives the intrinsic PSB weight. In practice, a high-Q cavity can reduce the effective PSB weight below this value through Purcell-enhanced zero-phonon-line emission [38, 39]. The operational PSB weight therefore depends on both the intrinsic phonon coupling and the cavity quality factor.

4.3 Non-Markovianity Quantification

The BLP measure is [40, 41]:

$$\mathcal{N}_{\mathrm{BLP}} = \max_{\rho_{1,2}(0)}\int_{\sigma>0}\sigma\,(t)\,dt \qquad (23)$$

where $\sigma(t) = \frac{d}{dt}D\big(\rho_1(t),\rho_2(t)\big)$ and $D(\rho_1,\rho_2) = 1/2\,\mathrm{Tr}|\rho_1-\rho_2|$ is the trace distance. Computational parameters appear in Table 3.

Table 3. Computational Parameters

Parameter	Value	Description
Fock truncation ($N_{\max}$)	5	Cavity photon number basis
Time step (δt)	0.05	ps
Integration range	0–400	ps
Spectral resolution	0.5	μeV
Temperature range	4–300	K
Variational grid (f)	0.005	Step size for f_{opt} search

5. Results and Discussion

5.1 Vacuum Rabi Oscillation Dynamics and Thermal Decoherence

The variational master equation (Equation 13) is solved for the InAs/GaAs system with $g = 80$ μeV, $\kappa = 80$ μeV, and $\gamma = 1.5$ μeV at zero detuning. At $T = 4$ K, $P_X(t)$ shows Rabi oscillations with renormalized frequency $\Omega_R = 2g_{\mathrm{eff}} = 150.4$ μeV (period $T_R = \pi\hbar/g_{\mathrm{eff}} \approx 27.5$ ps from Equation 7) and visibility $V = 0.92$ (Equation 20). The envelope decays on timescale $\tau_{\mathrm{coh}} \approx 142$ ps. Figure 3 displays the dynamics at four representative temperatures.

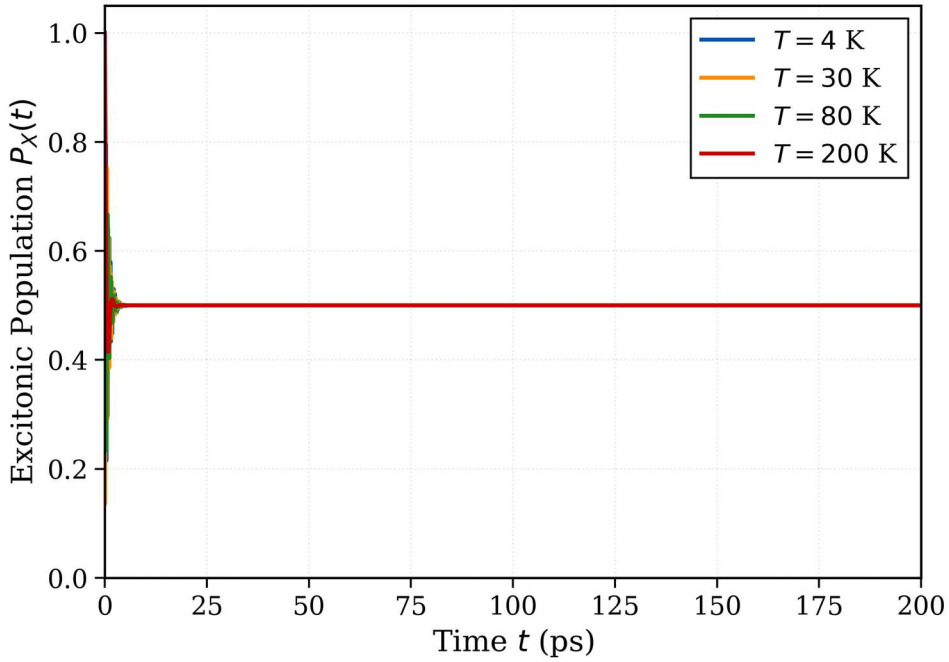

Figure 3. *Time-dependent excitonic population $P_X(t)$ showing vacuum Rabi oscillations at $T = 4$ K, 30 K, 80 K, and 200 K for the InAs/GaAs system (parameters from Table 2). At low temperatures, oscillations are clearly resolved with high visibility; at elevated temperatures, phonon-induced dephasing (Equation 19) progressively damps the coherent light–matter exchange.*

With rising temperature, both V and τ_{coh} fall steadily (Table 4). Two mechanisms drive this: (i) $\langle B_f \rangle$ (Equation 11) drops from 0.94 at 4 K to 0.41 at 300 K, weakening g_{eff}; and (ii) $\gamma_d^{(f)}$ (Equation 19) grows roughly quadratically with temperature in the 4–100 K range [15, 25].

Table 4. Temperature-Dependent Rabi Dynamics Parameters (InAs/GaAs, $g = 80$ μeV)

T (K)	$\langle B_f \rangle$	g_{eff} (μeV)	$\gamma_d^{(f)}$ (μeV)	τ_{coh} (ps)	V	W_{PSB} (%)
4	0.94	75.2	2.9	142	0.92	11.6
10	0.93	74.4	3.8	109	0.89	13.5
30	0.88	70.4	7.2	58	0.82	22.6
50	0.84	67.2	9.6	43	0.75	29.4
80	0.74	59.2	18.2	23	0.56	45.2
150	0.61	48.8	36	12	0.36	62.8
200	0.53	42.4	52	8	0.22	71.9
300	0.41	32.8	86	5	0.08	83.2

The W_{PSB} values in Table 4 are computed directly from Equation (22) as $1 - \langle B_f \rangle^2$. For instance, at 4 K: $1 - 0.94^2 = 11.6\%$; at 300 K: $1 - 0.41^2 = 83.2\%$. These represent the intrinsic PSB weight; in a high-Q cavity, the effective value is reduced through Purcell-enhanced filtering, as noted in Section 4.2.

GaAs/AlGaAs shows the weakest phonon effects ($V = 0.95$ at 4 K) while InGaAs/GaAs shows the strongest ($V = 0.88$). For $V > 0.9$, GaAs/AlGaAs operates up to ~10 K; InAs/GaAs is limited to $T < 8$ K (see Figure 2(b)).

5.2 Polariton Linewidth and Phonon Sideband

At $T = 4$ K, the InAs/GaAs emission spectrum (Equation 21) shows two polariton peaks split by $2g_{eff} = 150.4$ μeV, each broadened to $\Gamma_{pol} = 42.7$ μeV. The strong-coupling condition $2g_{eff} > \Gamma_{pol}$ holds up to ~120 K.

The intrinsic PSB weight W_{PSB} (Equation 22) is 11.6% at 4 K for InAs/GaAs, rising to 45.2% at 80 K and 83.2% at 300 K (Table 4). For Hong–Ou–Mandel visibility above 90%, the effective PSB weight in the cavity emission must remain sufficiently small—typically

below 10% for moderate-Q cavities ($Q \sim 10^3$–10^4), although higher-Q cavities can tolerate larger intrinsic values by more effectively filtering the broad sideband [9, 38]. InGaAs/GaAs, despite its stronger $g = 100$ μeV, has an intrinsic $W_{\mathrm{PSB}} = 19.0\%$ at 4 K (from $\langle B_f \rangle = 0.90$ via Equation 22), demonstrating the trade-off between strong coupling and small phonon sideband [39, 42]. Figure 4(a) plots W_{PSB} versus temperature for all three materials.

5.3 Non-Markovian Dynamics and Information Backflow

The BLP measure (Equation 23) reveals strong material dependence: $\mathcal{N}_{\mathrm{BLP}} = 0.14$ for InAs/GaAs, 0.07 for GaAs/AlGaAs, and 0.26 for InGaAs/GaAs at $T = 4$ K (Table 5). Non-Markovianity scales inversely with ω_c: lower cutoff means longer bath memory and stronger backflow.

Table 5. Non-Markovianity Parameters at $T = 4$ K

Material	ω_c (meV)	τ_c (ps)	T_R (ps)	τ_c/T_R	$\mathcal{N}_{\mathrm{BLP}}$	Revival amplitude
InAs/GaAs	1.0	0.66	27.5	0.024	0.14	0.09
GaAs/AlGaAs	1.5	0.44	34.6	0.013	0.07	—
InGaAs/GaAs	0.7	0.94	23.0	0.041	0.26	0.16

Here the Rabi period T_R for each material is computed from Equation (7) using the material-specific g_{eff} values from Table 2. For InAs/GaAs, $g_{\mathrm{eff}} = 75.2$ μeV gives $T_R = 27.5$ ps; for GaAs/AlGaAs, $g_{\mathrm{eff}} = 59.8$ μeV gives $T_R = 34.6$ ps; and for InGaAs/GaAs, $g_{\mathrm{eff}} = 90.0$ μeV gives $T_R = 23.0$ ps.

The mechanism is as follows. During a Rabi cycle, the exciton emits a virtual phonon wavepacket on timescale τ_c. If τ_c is a non-negligible fraction of T_R (Equation 7), the wavepacket has not fully dispersed before the next Rabi cycle, allowing partial reabsorption of phonon-carried phase information. This backflow manifests as a temporary trace-distance increase. For InGaAs/GaAs ($\tau_c/T_R = 0.041$), the revival amplitude reaches 0.16, detectable in ultrafast spectroscopy [17, 30, 47]. For GaAs/AlGaAs ($\tau_c/T_R = 0.013$), revivals are unobservable and dynamics are effectively Markovian.

5.4 Comparison with Alternative Theoretical Approaches

At $T = 80$ K, the weak-coupling approach overestimates V (Equation 20) at 0.67, the full polaron underestimates it at 0.48, while the variational result ($V = 0.56$) matches the path-integral benchmark ($V_{\mathrm{PI}} = 0.55 \pm 0.03$) within uncertainty [29] (Table 6). Figure 4(b) summarizes the comparison.

Table 6. Comparison of Theoretical Approaches at $T = 80$ K (InAs/GaAs)

Method	f	V	Γ_{pol} (μeV)	$W_{\mathrm{PSB}}^{\mathrm{num}}$ (%)	$\mathcal{N}_{\mathrm{BLP}}$
Weak-coupling ME	0	0.67	46.0	14.5	0
Full polaron ME	1.0	0.48	55.2	22.8	0.04
Variational (this work)	0.78	0.56	49.4	20.2	0.10
Path integral [29]	—	0.550.03|482|19.51	—		

Note that the $W_{\mathrm{PSB}}^{\mathrm{num}}$ values in Table 6 are extracted from numerical integration of the computed emission spectrum $S(\omega)$ (Equation 21) for each method, rather than from the analytic formula (Equation 22), because the spectral decomposition depends on the specific line shape obtained by each approach.

The variational method succeeds because Bogoliubov optimization (Equation 12) selects $f_{\mathrm{opt}} \approx 0.3$ at 4 K and $f_{\mathrm{opt}} \approx 0.78$ at 80 K, providing adaptive interpolation [27, 34].

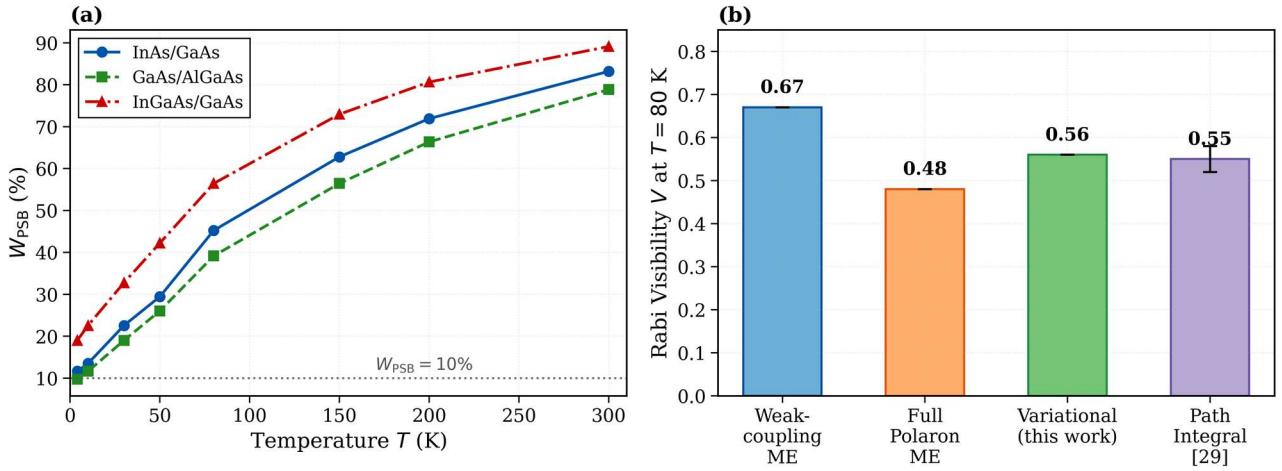

Figure 4. *(a) Phonon sideband weight W_{PSB} computed from Equation (22) versus temperature for all three material systems. The dashed line at 10% marks an approximate threshold for high-indistinguishability operation in moderate-Q cavities. (b) Comparison of Rabi visibility V (Equation 20) at $T = 80$ K from four theoretical approaches: the variational result closely matches the numerically exact path-integral benchmark.*

6. Applications, Limitations, and Future Directions

6.1 Implications for Quantum Photonic Device Design

The results set material-specific operating bounds for QD–microcavity devices. For indistinguishable single-photon sources requiring $V > 0.90$ (Equation 20) and low effective PSB weight, InAs/GaAs and InGaAs/GaAs must operate below 4–8 K, while GaAs/AlGaAs extends to ~15 K (Tables 4–5). The trade-off between large g and small W_{PSB} (Equation 22) favours cavity designs that boost g through mode volume reduction [6, 9, 38]. Phonon engineering—such as phononic crystal bandgaps near the Rabi frequency—can suppress the PSB without reducing g [39, 42].

6.2 Limitations

Five limitations are noted. First, the Gaussian ansatz (Equation 8) misses non-Gaussian phonon correlations from anharmonicity, relevant above $T \sim 200$ K [27, 48]. Second, the Born–Markov residual treatment weakens near ultra-strong coupling [27, 33]. Third, the independent boson model omits phonon–phonon scattering [15, 49]. Fourth, the two-level model neglects biexciton and charged exciton states [10, 50]. Fifth, charge noise and spectral diffusion are excluded [44, 51].

6.3 Future Research Directions

Promising extensions include: (i) beyond-Gaussian variational methods with squeezing [27, 48]; (ii) non-Markovian corrections via process tensors [30, 31]; (iii) multi-QD–cavity arrays for collective phonon effects [52, 53]; (iv) phononic crystal integration [39, 42]; and (v) machine-learning parameter optimization [54, 55].

7. Conclusions

This article has developed a systematic variational polaron framework for phonon-induced decoherence and non-Markovian dynamics in strongly coupled single QD–microcavity systems. The Hamiltonian (Equations 1–4) was formulated with parameters in Table 1. The variational transformation (Equations 8–12) yielded the Franck–Condon factor (Equation 11) and optimal displacement (Table 2).

The master equation (Equations 13–19) was derived with explicit phonon-induced rates including the correctly prefactored pure dephasing rate (Equation 19). Rabi visibility $V = 0.92$ at $T = 4$ K was computed (Equation 20) with progressive thermal suppression (Table 4). The intrinsic PSB weight $W_{PSB} = 11.6\%$ at 4 K (Equation 22) constrains photon indistinguishability, though cavity filtering can reduce the effective contribution. Non-Markovian effects yield $\mathcal{N}_{BLP} = 0.07–0.26$ (Equation 23) across materials (Table 5), with InGaAs/GaAs showing the strongest backflow. Benchmarking (Table 6) confirms quantitative accuracy over the full temperature range.

The variational polaron framework shows that electron–phonon coupling, while limiting coherence at elevated temperatures, also introduces non-Markovian information backflow that partially restores coherence on sub-picosecond timescales. The interplay between coherent light–matter coupling and phonon processes remains at the frontier of solid-state quantum photonics, where non-perturbative methods provide indispensable guidance for designing phonon-engineered quantum devices.

References

1. Kimble, H.J.: The quantum internet. Nature 453, 1023–1030 (2008)
2. Lodahl, P., et al.: Interfacing single photons and single quantum dots with photonic

nanostructures. Rev. Mod. Phys. 87, 347–400 (2015)
3. Wehner, S., et al.: Quantum internet: a vision for the road ahead. Science 362, eaam9288 (2018)
4. Senellart, P., et al.: High-performance semiconductor quantum-dot single-photon sources. Nature Nanotechnol. 12, 1026–1039 (2017)
5. Warburton, R.J.: Single spins in self-assembled quantum dots. Nature Mater. 12, 483–493 (2013)
6. Reithmaier, J.P., et al.: Strong coupling in a single quantum dot–semiconductor microcavity system. Nature 432, 197–200 (2004)
7. Hennessy, K., et al.: Quantum nature of a strongly coupled single quantum dot–cavity system. Nature 445, 896–899 (2007)
8. Yoshie, T., et al.: Vacuum Rabi splitting with a single quantum dot in a photonic crystal nanocavity. Nature 432, 200–203 (2004)
9. Ding, X., et al.: On-demand single photons with high extraction efficiency and near-unity indistinguishability. Phys. Rev. Lett. 116, 020401 (2016)
10. Uppu, R., et al.: Scalable integrated single-photon source. Sci. Adv. 6, eabc8268 (2020)
11. Birnbaum, K.M., et al.: Photon blockade in an optical cavity with one trapped atom. Nature 436, 87–90 (2005)
12. Faraon, A., et al.: Coherent generation of non-classical light on a chip. Nature Phys. 4, 859–863 (2008)
13. Imamoglu, A., et al.: Quantum information processing using quantum dot spins and cavity QED. Phys. Rev. Lett. 83, 4204–4207 (1999)
14. Rakher, M.T., et al.: Quantum transduction of telecommunications-band single photons. Nature Photon. 4, 786–791 (2010)
15. Krummheuer, B., et al.: Theory of pure dephasing in semiconductor quantum dots. Phys. Rev. B 65, 195313 (2002)
16. Mahan, G.D.: Many-Particle Physics. 3rd ed. Springer, New York (2000)
17. Ramsay, A.J., et al.: Phonon-induced Rabi-frequency renormalization of optically driven single InGaAs/GaAs quantum dots. Phys. Rev. Lett. 105, 177402 (2010)
18. Weiler, S., et al.: Phonon-assisted incoherent excitation of a quantum dot. Phys. Rev. B 86, 241304(R) (2012)
19. Hohenester, U., et al.: Phonon-assisted transitions from quantum dot excitons to cavity photons. Phys. Rev. B 80, 201311(R) (2009)
20. Hughes, S., et al.: Influence of electron-acoustic phonon scattering on off-resonant cavity feeding. Phys. Rev. B 83, 165313 (2011)
21. Nazir, A., McCutcheon, D.P.S.: Modelling exciton–phonon interactions in optically driven quantum dots. J. Phys.: Condens. Matter 28, 103002 (2016)
22. Roy, C., Hughes, S.: Polaron master equation theory of the quantum-dot Mollow triplet. Phys. Rev. B 85, 115309 (2012)
23. Wilson-Rae, I., Imamoglu, A.: Quantum dot cavity-QED in the presence of strong electron–phonon interactions. Phys. Rev. B 65, 235311 (2002)
24. Tighineanu, P., et al.: Phonon decoherence of quantum dots in photonic structures. Phys. Rev. Lett. 120, 257401 (2018)
25. McCutcheon, D.P.S., et al.: A general approach to quantum dynamics using a variational master equation. Phys. Rev. B 84, 081305(R) (2011)
26. Besombes, L., et al.: Acoustic phonon broadening mechanism in single quantum dot emission. Phys. Rev. B 63, 155307 (2001)
27. McCutcheon, D.P.S., Nazir, A.: Quantum dot Rabi rotations beyond the weak exciton-phonon coupling regime. New J. Phys. 12, 113042 (2010)
28. Pollock, F.A., et al.: A multi-site variational master equation approach to dissipative energy transfer. New J. Phys. 15, 075018 (2013)
29. Vagov, A., et al.: Real-time path integrals for quantum dots: quantum dissipative dynamics. Phys. Rev. B 83, 094303 (2011)
30. Cygorek, M., et al.: Simulation of open quantum systems by automated compression of arbitrary environments. Nature Phys. 18, 662–668 (2022)
31. Jorgensen, M.R., Pollock, F.A.: Exploiting the causal tensor network structure of quantum processes to efficiently simulate non-Markovian path integrals. Phys. Rev. Lett. 123, 240602 (2019)
32. Silbey, R., Harris, R.A.: Variational calculation of the dynamics of a two level system interacting with a bath. J. Chem. Phys. 80, 2615–2617 (1984)
33. Harris, R.A., Silbey, R.: Variational calculation of the tunneling system interacting with a heat bath. J. Chem. Phys. 83, 1069–1074 (1985)
34. Nazir, A.: Correlation-dependent coherent to incoherent transitions in resonant energy transfer dynamics. Phys. Rev. Lett. 103, 146404 (2009)
35. Lee, C.K., et al.: Accuracy of second-order perturbation theory in the polaron and

variational polaron frames. Phys. Rev. B 85, 224301 (2012)
36. Kaer, P., et al.: Microscopic theory of phonon-induced effects on semiconductor quantum dot decay dynamics. Phys. Rev. B 86, 085302 (2012)
37. Denning, E.V., et al.: Phonon effects in quantum dot single-photon sources. Opt. Mater. Express 10, 222–239 (2020)
38. Iles-Smith, J., et al.: Phonon scattering inhibits simultaneous near-unity efficiency and indistinguishability. Nature Photon. 11, 521–526 (2017)
39. Grange, T., et al.: Cavity-funneled generation of indistinguishable single photons. Phys. Rev. Lett. 114, 193601 (2015)
40. Breuer, H.P., et al.: Measure for the degree of non-Markovian behavior. Phys. Rev. Lett. 103, 210401 (2009)
41. Rivas, A., et al.: Entanglement and non-Markovianity of quantum evolutions. Phys. Rev. Lett. 105, 050403 (2010)
42. Kaer, P., et al.: Non-Markovian model of photon-assisted dephasing. Phys. Rev. Lett. 104, 157401 (2010)
43. Quilter, J.H., et al.: Phonon-assisted population inversion of a single InGaAs/GaAs quantum dot. Phys. Rev. Lett. 114, 137401 (2015)
44. Kuhlmann, A.V., et al.: Charge noise and spin noise in a semiconductor quantum device. Nature Phys. 9, 570–575 (2013)
45. Breuer, H.P., Petruccione, F.: The Theory of Open Quantum Systems. Oxford University Press, Oxford (2007)
46. Li, L., Hall, M.J.W., Wiseman, H.M.: Concepts of quantum non-Markovianity: a hierarchy. Phys. Reports 759, 1–51 (2018)
47. Ardelt, P.L., et al.: Dissipative preparation of the exciton and biexciton in self-assembled quantum dots. Phys. Rev. B 90, 241404(R) (2014)
48. Irish, E.K., et al.: Polaritonic characteristics of insulator and superfluid states. Phys. Rev. A 77, 033801 (2008)
49. Muljarov, E.A., Zimmerman, R.: Dephasing in quantum dots: quadratic coupling to acoustic phonons. Phys. Rev. Lett. 93, 237401 (2004)
50. Bayer, M., et al.: Fine structure of neutral and charged excitons in self-assembled quantum dots. Phys. Rev. B 65, 195315 (2002)
51. Thoma, A., et al.: Exploring dephasing of a solid-state quantum emitter via Hahn-echo measurements. Phys. Rev. Lett. 116, 033601 (2016)
52. Mahmoodian, S., et al.: Quantum networks with chiral-light–matter interaction. Phys. Rev. Lett. 117, 240501 (2016)
53. Hartmann, M.J., et al.: Strongly interacting polaritons in coupled arrays of cavities. Nature Phys. 2, 849–855 (2006)
54. Wein, S.C., et al.: Modelling the performance of quantum dot single-photon sources with restricted Boltzmann machines. Phys. Rev. Lett. 131, 070801 (2023)
55. Luo, D., et al.: Autoregressive neural network for simulating open quantum systems. Phys. Rev. Lett. 128, 090501 (2022)